

Restyling Unsupervised Concept Based Interpretable Networks with Generative Models

Jayneel Parekh^{*1,2}, Quentin Bouniot^{*2}, Pavlo Mozharovskyi², Alasdair Newson¹, and Florence d’Alché-Buc²

¹ ISIR, Sorbonne Université

² LTCI, Télécom Paris, Institut Polytechnique de Paris, France

Abstract. Developing inherently interpretable models for prediction has gained prominence in recent years. A subclass of these models, wherein the interpretable network relies on learning high-level concepts, are valued because of closeness of concept representations to human communication. However, the visualization and understanding of the learnt unsupervised dictionary of concepts encounters major limitations, specially for large-scale images. We propose here a novel method that relies on mapping the concept features to the latent space of a pretrained generative model. The use of a generative model enables high quality visualization, and naturally lays out an intuitive and interactive procedure for better interpretation of the learnt concepts. Furthermore, leveraging pretrained generative models has the additional advantage of making the training of the system more efficient. We quantitatively ascertain the efficacy of our method in terms of accuracy of the interpretable prediction network, fidelity of reconstruction, as well as faithfulness and consistency of learnt concepts. The experiments are conducted on multiple image recognition benchmarks for large-scale images. Project page available at https://jayneelparekh.github.io/VisCoIN_project_page/

Keywords: Interpretability · Explainability · Generative models

1 Introduction

Deep neural networks (DNNs) learn complex patterns from data to make predictions or decisions without being explicitly programmed how to perform the task. *Interpreting* decisions of DNNs, *i.e.* being able to obtain human-understandable insights about their decisions, is a difficult task [11, 13, 49]. This lack of transparency impacts their trustworthiness [58] and hinders their democratization for critical applications such as assisting medical diagnosis or autonomous driving.

Two different paths have been explored in order to interpret DNNs outputs. The simplest approach for practitioners is to provide interpretations *post-hoc*, *i.e.* by analysing the so-called *black-box* model *after* training [12, 47, 55, 61]. However, *post-hoc* methods have been criticized for their high computational costs and a lack of robustness and faithfulness of interpretations [8, 37, 78]. On

* Equal contribution

the other hand, one preferred way to obtain more meaningful interpretations is to use *interpretable by-design* approaches [3, 5, 14, 21], that aim to integrate the interpretability constraint into the learning process, while maintaining state-of-the-art performance.

Concept-based Interpretable Networks (CoINs) are a recent subcategory of these inherently interpretable prediction models, that learn a dictionary of *high-level concepts* for prediction. The concept representation is either learnt in a supervised way using ground-truth concepts annotations [40, 59], or in an unsupervised fashion by enforcing properties through carefully designed loss functions [7, 51, 59]. The output of the model can be interpreted by looking at the *activations* of each concept and how they are combined to obtain the final prediction. When working in the unsupervised setting, learnt concepts have to additionally be interpreted, usually through *visualization* [51, 59]. *Concept-based interpretations* have gained prominence as an alternative to popular feature-wise saliency maps [47, 55, 61, 66] for two main reasons: (1) their ability to provide interpretations closer to human reasoning and communication [76], and (2) in specific case of visual modalities, their ability to more effectively highlight *which* features are important for a model and not just *where* in the input image they focus on [16]. However, the underlying concepts in current unsupervised CoINs are understood through a *separate visualization pipeline*, by finding inputs that highly activate a given concept, either from natural images in the available dataset [7, 59], or from virtual images by solving an optimization problem in the input space that maximally activates the concept [48, 51]. For large-scale images, concepts generally activate for local pattern information (color, texture, shape etc.) and these visualization approaches face major limitations in highlighting this information to a user. Simply visualizing the most activating samples does not highlight the specific feature a concept activates for. Visualizing using an activation maximization procedure leads to the generation of repeated patterns linked to the underlying concept in the image, but are hard for a user to discern any human-interpretable signal. For example, in Fig. 1, it can be hard to identify that the concept activates for “Yellow-colored head” from the activation maximization (“FLINT visualization”). Furthermore, previous CoIN systems fail to include the visualization process in their quantitative evaluation of concepts.

We thus propose a novel set of specifications for the concepts to be learnt: additionally to *fidelity to output* (predictive capability from the concepts), *fidelity to input* (encoding input relevant information in concepts) and *sparsity* (a few concepts activated simultaneously), we also promote the *viewability* of concepts during training. This viewability is now defined as the ability of the system to reconstruct *high-quality* images from the learnt concepts, by leveraging a *pretrained generative model*. In order to obtain this viewability property, we propose to learn a *concept translator*, *i.e.*, a *mapping* from the *concept representation space* to the latent space of the generative model. Learning the concept translator along with the other parameters of this novel CoIN system helps to improve the quality of the concepts. Finally, after training, interpretation of con-

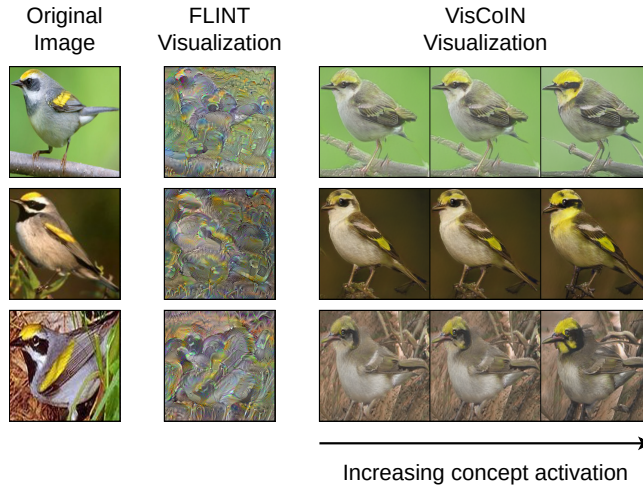


Fig. 1: Comparison of the generated images obtain for the same learnt concept (“Yellow-colored head”) using FLINT visualization [51] and our proposed VisCoIN visualization. Using our *concept translator*, that maps concept representation space to the latent space of a generative model, we can visualize each concept at different activation values, allowing for more granular and interactive interpretation.

cepts is obtained through *translation* to the generative model, which allows for a more granular and interactive process. Our contributions are the following:

- (i) We propose *Visualizable CoIN (VisCoIN)*, a novel architecture for unsupervised training of CoINs relying on a *concept translator* module that maps concept vectors to the latent space of a pretrained generative model.
- (ii) We introduce a new property for unsupervised CoIN systems, related to *viewability*. This property is imposed during the training of the system by enforcing *perceptual similarity* of the reconstruction, in addition to other constraints, and made possible by the use of a generative model.
- (iii) We define a novel concept interpretation pipeline based on the concept translator and the associated generative model that allows to both obtain a high-quality and more comprehensive visualization of each concept.
- (iv) We introduce new metrics in the context of unsupervised CoINs to evaluate the quality of concepts learnt, from the point of view of *visualization*. We then quantitatively and qualitatively evaluate our proposed method on three different large-scale image datasets, spanning multiple settings.

2 Related works

Interpretable predictive models In the context of deep learning architectures, a host of early approaches studying interpretability tackled the post-hoc interpretation problem [15, 47, 55, 63, 66, 67]. However, previous works such as

those of [5, 7, 45] have contributed to surge of developing predictive models that are also interpretable *by-design* [4, 21, 44, 77, 81]. The earlier systems however trained the complete model from scratch. Recent approaches reflect a growing interest in building interpretable models on top of pretrained models as backbones [9, 40]. Our approach falls in the latter category wherein we learn an interpretable predictive model on top of a pretrained backbone.

GANs for interpretations One of the earliest application of GANs for interpretability was by [50] to synthesize image for visualizing neurons in a network. More recently, a variety of methods have employed GAN or other generative models (including diffusion models) for generating post-hoc counterfactual interpretations [19, 22, 43, 80]. Their central theme revolves around the idea of embedding any given input to the latent space of a GAN and finding meaningful perturbations in the latent space that affect the given predictor’s output the most. Our aimed use-case of the GAN differs in a major way from these methods, which is that we wish to use the GAN in order to learn and visualize an explicit dictionary of interpretable concept representation simultaneously used in a predictive model.

Concept-based interpretability Providing interpretations via representations for high-level *concepts* has gained significant prominence recently. Similar to the overall literature, one set of concept-based methods have focused on post-hoc interpretation [2, 20, 23, 43, 76], with most based on the notion of concept activation vectors [36]. The other type of methods tackle the by-design/ante-hoc interpretation problem by learning concepts [7, 40, 51, 59, 60, 62] abbreviated as CoIN systems in Sec. 1. We cover these methods in more detail in Sec. 3.1 with particular focus on networks based on learning completely unsupervised concepts [7, 51, 59], a key starting point of our approach.

3 Approach

3.1 Background

In this part, we provide a design overview of a concept based interpretable network (CoIN). Our focus in this paper is on CoIN systems that learn an unsupervised dictionary of concepts.

Concept-based interpretable networks We denote a training set for a supervised image classification task as $\mathcal{S} = \{(x_i, y_i)\}_{i=1}^N$. Each input image $x \in \mathcal{X} \subset \mathbb{R}^n$ is associated with a class label $y \in \mathcal{Y}$, a one-hot vector of size number of classes C . The *by-design interpretable network* based on learning concept representation is denoted by $g : \mathcal{X} \rightarrow \mathcal{Y}$.

In the standard setup for concept-based prediction models (supervised or unsupervised), given an input x , the computation of $g(x)$ is broken down into two parts. There is first a *concept extraction representation* Φ , and then a subnetwork Θ that computes the final prediction using *concept activations* $\Phi(x)$, such that $g(x) = \Theta \circ \Phi(x)$. *Supervised* concept-based networks [40] use *ground-truth concept annotations* to train Φ . The core of *unsupervised* concept-based methods instead

lies in learning Φ by imposing *loss functions*. These loss functions are typically selected to encourage a certain set of properties that shape Φ simultaneously for both interpretation and prediction. We list the properties below:

1. **Fidelity to output:** This requires $\Phi(x)$ to model the output space via the Θ function, either by predicting ground-truth label y [7] or the classification output $f(x)$ [51, 59]. It directly shapes $\Phi(x)$ for the prediction task and, during the interpretation phase, it helps in identifying important concepts for prediction.
2. **Fidelity to input:** This requires $\Phi(x)$ to reconstruct the input x via a *decoder* function. This property is essential to encode features relevant to the input in the concept representation. All the previous methods [7, 51, 59] rely on this loss and employ standard *non-generative* decoders for pixel-wise reconstruction to learn the concept dictionary Φ .
3. **Sparsity of activations:** This requires concept activations $\Phi(x)$ to be sparse for any x . It reinforces the high-level nature of Φ and limits the number of important concepts for prediction, in turn enhancing interpretability as well as reducing the visualization overhead for a user.

Limitations with concept visualization in previous unsupervised CoINs

A central common trait among prior CoINs learning unsupervised concepts [7, 51, 59] is the deployment of a decoder to reconstruct input x from $\Phi(x)$. Unlike supervised methods, they do not have access to any concept labels and thus need an additional visualization pipeline to understand the information encoded by each concept. However, their visualization pipeline does not utilize the decoder, but instead relies on proxy methods to probe the concept activation. Typically, it consists of finding an input that highly activates a concept, either by selecting from the training data [7, 59] or via input optimization [51]. In the former case, simply visualizing the set of most activating training samples lacks granularity to highlight the features encoded by the concept. Using input optimization, while relatively more insightful, is still difficult for a user to understand as the optimized images are often unnatural. Moreover, these issues exacerbate for large-scale images, as seen in Fig. 1. A natural strategy to overcome these limitations is to enable direct control of a concept’s activation and visualizing its effect on the input. Since the decoder defines the relationship between concept activations and input samples, a *generative model* is a perfect candidate for a decoder to unlock this ability, in contrast to standard decoders used previously.

In the next part, we describe the architecture behind our *by-design interpretable network* g , that additionally includes a *concept translator* module Ω , to map concept features in the latent space of a pretrained generative model G . This defines our *VisCoIN* method.

3.2 Interpretable prediction network design

We assume a fixed pretrained network for classification f and a fixed pretrained generator G , trained for classification and generation on input dataset respectively. We use these two networks to guide our design and learning of g and its

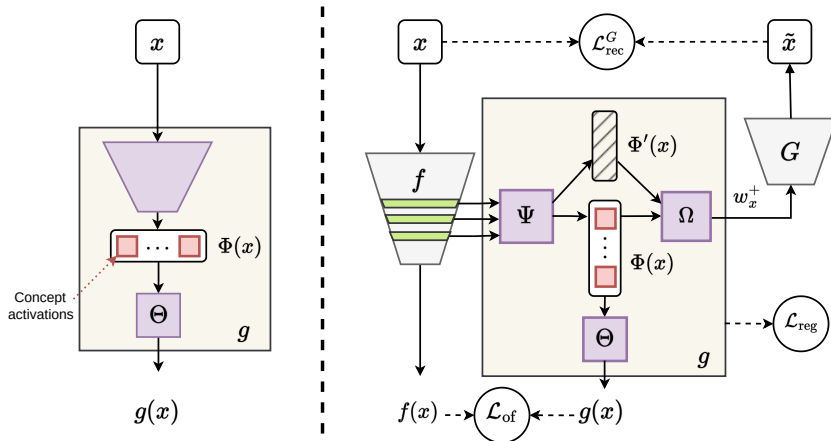


Fig. 2: **Left:** Overview of a standard CoIN system g , that makes prediction $g(x)$ from extracted concepts $\Phi(x)$. **Right:** Design of our unsupervised concept-based interpretable network *VisCoIN* leveraging a pretrained generative model G for visualization, and a pretrained classifier f . Purple blocks denote trainable subnetworks.

concept extraction function Φ . We first discuss modelling of g by describing its constituents, Φ and Θ .

Interpretable network design The *dictionary* Φ consists of K *concept functions* ϕ_1, \dots, ϕ_K . Given an input x , each concept activation $\phi_k(x)$ is represented by a small convolutional feature map with non-negative activation. Thus $\Phi(x) = [\phi_1(x), \dots, \phi_K(x)] \in \mathbb{R}_+^{K \times b}$, where b is the total number of elements in each feature map. We model computation of concept activations $\Phi(x)$ using the pretrained classification network f and learn a relatively lightweight network Ψ on top of its selected hidden layers denoted as $f_{\mathcal{I}}(x)$, *i.e.* $\Phi(x) = \Psi \circ f_{\mathcal{I}}(x)$. Θ is designed to simply pool the feature maps to obtain a single concept activation of size K and make the final prediction by passing it through a linear layer followed by softmax, *i.e.* $g(x) = \Theta(\Phi(x)) = \text{softmax}(\Theta_W^T \text{pool}(\Phi(x)))$, where $\Theta_W \in \mathbb{R}^{K \times C}$ are the weights in the linear layer. The simplified design of Θ makes estimating importance of each concept function ϕ_k for any prediction straightforward.

Viewability property In order to improve visualization for unsupervised CoINs, and thus interpretation of learnt concepts, we propose to add the requirement for a *viewability property*. Given an input image x , this property requires to be able to reconstruct *high-quality* images from $\Phi(x)$, from a pretrained generative model G . More specifically, reconstructions should have high enough quality to “view” input samples through generated outputs and thus ground modifications to $\Phi(x)$ back to x . In our method, we propose to achieve this by learning an additional *concept translator* module Ω to map $\Phi(x)$ to the latent space of G , such that high-quality reconstructed images can be obtained from $\Phi(x)$ through Ω and G . The design of Ω depends entirely on the generative model used.

We opt for StyleGAN2-ADA [31] as our generative model. Our rationale behind this choice is due to certain properties exhibited by this model: (a) a low

dimensional and highly structured latent space with meaningful transformations in generated output via latent traversals, (b) can generate high-quality large-scale images, and (c) flexible to train in limited data regimes. We discuss about the significance of these properties and suitability of other generative models in much greater detail in Appendix A.1. It’s worth noting that using a pretrained generator also limits the training cost, complexity and improves reusability.

3.3 Use of StyleGAN as decoder

A short primer on style-based GAN The work by Karras et al. [33] proposed a style-based generator architecture. The generator learns to map a noise vector ($z \in \mathbb{R}^{512} \sim \mathcal{N}(0, 1)$) to a latent code ($w \in \mathcal{W} \subset \mathbb{R}^{512}$) that controls the scaling and biasing of feature maps at different resolutions in the synthesis network, controlling the style of the generated image. Subsequent updates on the original architecture [32, 34] have improved upon various aspects of generator architecture and regularization. One such update relevant for us is the StyleGAN2-ADA [31] which incorporates an adaptive discriminator augmentation in training. This enables training StyleGAN2 with limited amount of data, a regime where GANs are generally prone to collapsing. The StyleGAN architecture has been actively studied for certain aspects relevant to our use case. Primary among these are GAN inversion methods that aim to embed any given input to the latent space of a pretrained GAN so that the GAN can reconstruct the input using the latent code. The two approaches for this include either optimizing a latent code for any given input [1, 29], or training an encoder to predict the latent code [6, 56, 75]. While the optimization approaches can invert a given input better, they scale poorly compared to encoder based approaches when inverting many input samples. StyleGAN has also been studied closely in regard to its structure of latent spaces, including their suitability to embed inputs [1, 72, 73], discovering semantically meaningful directions or trajectories in latent space [25, 65, 69] and hierarchical style control with latent vectors for different resolutions [35].

At this juncture, it is worth asking the question of why don’t we directly use the latent space/stylesheet [72] of the pretrained StyleGAN as the concept dictionary for interpretation, as done previously [43]. We discuss about this question in detail in Appendix A.2, including issues in this design for use in a by-design interpretable network. Instead, we adhere to standard setup for unsupervised CoINs to learn a small dictionary of concept functions. The pretrained StyleGAN is used to reconstruct input x from concept activations $\Phi(x)$.

The most natural way to design this reconstruction is to use a similar approach to encoder based GAN-inversion architectures used for StyleGAN. Following previous works in this regard [1, 75], we use the extended latent space \mathcal{W}^+ for inversion, which corresponds to different latent vectors for different resolutions. We learn the concept translator Ω to map the concept activations to \mathcal{W}^+ and bias its computation with average latent vector \bar{w} of G .

Since $\Phi(x)$ is a much lower dimensional representation compared to elements in \mathcal{W}^+ and constrained by losses unrelated to reconstruction, we found it chal-

lenging to achieve reconstruction quality close to GAN inversion methods. This issue in principle cannot be completely eliminated without compromising the interpretable predictive structure. However, we alleviate it to some extent by learning an unconstrained “supporting” representation as a secondary output from Ψ , termed $\Phi'(x)$. The only goal for $\Phi'(x)$ is to assist Ω in embedding the input in \mathcal{W}^+ . We utilize findings from the work in [35] about hierarchical nature of latent vectors and control prediction of small number of latent vectors using $\Phi'(x)$ which are expected to contain minimal classification related information. To ensure importance of $\Phi(x)$ in reconstruction is not diminished, majority of latent vectors are still predicted using $\Phi(x)$. The choice of using Φ' is analyzed with an ablation study. The computation for reconstructed input \tilde{x} is given as:

$$\tilde{x} = G(w_x^+), \text{ where } w_x^+ = \Omega(\Phi(x), \Phi'(x)) \in \mathcal{W}^+ \quad (1)$$

The concept translator Ω consists of a set of single fully-connected (FC) layers, one for predicting each latent vector. Each FC layer either takes $\Phi(x)$ or $\Phi'(x)$ as input depending upon the latent vector it predicts. Precise details about Ω and $\Phi'(x)$ are in Appendix B. Fig. 2 illustrates the complete design of VisCoIN.

3.4 Training losses

Based on the previous discussion about concept based networks and our reconstruction pipeline design inspired from GAN inversion architectures, we define here our training loss \mathcal{L}_{train} and each of its constitutive terms.

- To verify the *fidelity to output* property, we define an *output fidelity loss* \mathcal{L}_{of} , which grants predictive capabilities to g . It is defined as the generalized cross entropy (CE) loss between g and f :

$$\mathcal{L}_{of}(x; \Psi, \Theta) = \alpha CE(g(x), f(x)). \quad (2)$$

- The most critical part of our training loss is the *reconstruction loss* \mathcal{L}_{rec}^G computed through the pretrained generative model G , that gathers all constraints between inputs x and their reconstruction $\tilde{x} = G(\Omega(\Phi(x), \Phi'(x)))$. It combines ℓ_1 and ℓ_2 penalties, enforcing pixel-wise reconstruction for *fidelity to input*, with perceptual similarity LPIPS [82] and a final *reconstruction classification* term, both linked to *viewability*. The *reconstruction classification* term, defined as $CE(f(\tilde{x}), f(x))$, encourages the generative model to reconstruct \tilde{x} with more classification specific features pertaining to input x . Similar losses have been introduced for inversion with StyleGAN and its training for *post-hoc* interpretation [43]. Our reconstruction loss is thus defined as follows:

$$\mathcal{L}_{rec}^G(x; \Psi, \Omega) = \|\tilde{x} - x\|_2^2 + \|\tilde{x} - x\|_1 + \beta \text{LPIPS}(\tilde{x}, x) + \gamma CE(f(\tilde{x}), f(x)). \quad (3)$$

- We impose the *sparsity* property along with two other regularizations, combined under the term \mathcal{L}_{reg} . More specifically, Ψ is regularized to encourage

sparsity of activations in $\Phi(x)$ through an ℓ_1 penalty, and *diversity* while reducing *redundancy* in learnt dictionary Φ with a *kernel orthogonality* loss \mathcal{L}_{orth} , applied on weights of final convolution layer of Ψ [71, 74]. Then, Ω is encouraged to predict latent vectors close to average latent vector \bar{w} , a common practice in GAN-inversion systems [68]. The regularization terms are written as follows:

$$\begin{aligned} \mathcal{L}_{reg}(x; \Psi, \Omega) &= \mathcal{L}_{reg-\Psi}(x; \Psi) + \mathcal{L}_{reg-\Omega}(x; \Omega), \\ \mathcal{L}_{reg-\Omega}(x; \Omega) &= \|w_x^+ - \bar{w}\|_2^2, \quad \mathcal{L}_{reg-\Psi}(x; \Psi) = \delta \|\Phi(x)\|_1 + \mathcal{L}_{orth}(\Psi). \end{aligned} \quad (4)$$

Finally, the training loss and the optimization can be summarized as:

$$\begin{aligned} \mathcal{L}_{train}(x; \Psi, \Theta, \Omega) &= \mathcal{L}_{of}(x; \Psi, \Theta) + \mathcal{L}_{rec}^G(x; \Psi, \Omega) + \mathcal{L}_{reg}(x; \Psi, \Omega), \\ \hat{\Psi}, \hat{\Theta}, \hat{\Omega} &= \arg \min_{\Psi, \Theta, \Omega} \frac{1}{N} \sum_{x \in \mathcal{S}} \mathcal{L}_{train}(x; \Psi, \Theta, \Omega). \end{aligned} \quad (5)$$

In the above equations, the loss hyperparameters are denoted by $\alpha, \beta, \gamma, \delta$. During training, the overall training loss is simultaneously optimized w.r.t parameters of only Ψ, Θ and Ω , keeping f and G fixed.

3.5 Interpretation phase

We now describe the interpretation generation process, which can be divided in two parts. (1) **Concept relevance estimation**, that requires estimating the importance of any given concept function ϕ_k in prediction for a particular sample x (local interpretation) or a class c in general (global interpretation), and (2) **Concept visualization**, which pertains to visualizing the concept encoded by any given concept function ϕ_k . We describe each of them in greater detail below: (1) **Concept relevance:** Since our $g(x)$ adheres to structure of CoINs and among them closest to [51], the first step of relevance estimation almost follows as is. The estimation is based on concept activations $\Phi(x)$, and how the pooled version of $\Phi(x)$ is combined by the fully connected layer in Θ (with weights Θ_W) to obtain the output logits. Note that this step does not rely on using the decoder/generator G . Specifically, the local relevance $r_k(x)$ of a concept function ϕ_k for a given sample x is computed as the normalized version (between $[-1, 1]$) of its contribution to logit of the predicted class $\hat{c} = g(x)$. The global relevance of concept function ϕ_k for a given class c , denoted $r_{k,c}$, is computed as the average of local relevance $r_k(x)$ for samples from class c . The above description is summarized in equation below wherein $\Theta_W^{k,\hat{c}}$ denotes the weight on concept k for predicted class \hat{c} in weight matrix Θ_W :

$$r_k(x) = \frac{\alpha_k(x)}{\max_l |\alpha_l(x)|}, \quad \alpha_k(x) = \text{pool}(\phi_k(x)) \Theta_W^{k,\hat{c}}, \quad r_{k,c} = \mathbb{E}(r_k(x) | g(x) = c)$$

(2) **Concept visualization:** Once the importance of a concept function is estimated, one can extract the most important concepts for a sample x or class c by

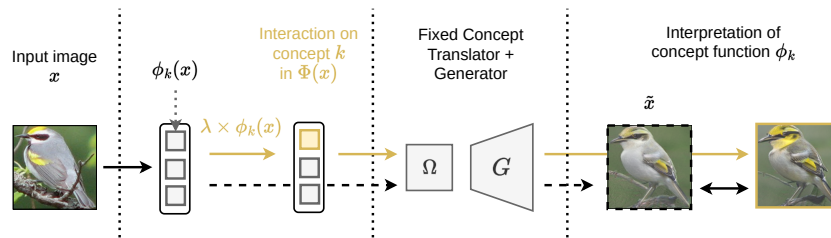


Fig. 3: Overview of visualization for a given image x and concept function ϕ_k . By inputting a higher activation for $\phi_k(x)$ in $\Phi(x)$ (by a factor $\lambda = 4$ in the figure), and comparing the obtained visualization to the original reconstruction \tilde{x} (obtained with the untouched $\Phi(x)$), we interpret information encoded by ϕ_k about image x . For simplicity, we omit $\Phi'(x)$ in the figure, as it remains the same.

thresholding $r_k(x)$ or $r_{k,c}$ respectively. For visualizing any concept ϕ_k , following previous CoINs, one can start by selecting most activating training samples for $\phi_k(x)$ over the whole training set or separately for each class it is highly relevant for. However, the core of our concept visualization process, is to utilize generator G to visualize the impact of ϕ_k on any input x it is relevant for. We do so by (1) directly modifying activation of $\phi_k(x)$ by a factor $\lambda \times \phi_k(x)$, $\lambda \geq 0$ while keeping all other activations in $\Phi(x)$ intact, and (2) Visualizing generated output for increasing value of λ . The case of $\lambda = 1$ corresponds to \tilde{x} , the reconstructed version of x . This process is summarized in Fig. 3. Extremely high values of λ can push the predicted latent vectors far from the average latent vector in which case the generated output is less reliable. For our experiments, qualitatively we found maximum λ upto 3 or 4 reliable with consistent modifications.

4 Experiments and Results

Datasets We experiment on image recognition tasks for large-scale images in three different domains with a greater focus on multi-class classification tasks: (1) Binary age classification (young/old) on CelebA-HQ [30], (2) fine-grained bird classification for 200 classes on Caltech-UCSD-Birds-200 (CUB-200) [70], and (3) fine-grained car model classification of 196 classes on Stanford Cars [41].

Implementation details We use a ResNet50 [26] as our architecture for f . All images are processed at resolution 256×256 . For the pretrained GAN, on CelebA-HQ we use checkpoint released by NVIDIA [31]. On CUB-200 and Stanford Cars, we fine-tune an ImageNet [24] and LSUN Cars [79] checkpoint respectively to obtain the pretrained G in a resource efficient manner. The fine-tuning is performed without any class-labels. We use a dictionary size $K = 64$ on CelebA-HQ and $K = 256$ on CUB-200 and Stanford-Cars. All experiments were conducted on a single V100-32GB GPU. Complete details about architecture, training and evaluation are in appendix B.

We will release our code publicly upon publication.

4.1 Evaluation strategy

One major goal of by-design interpretable architectures is to obtain high prediction performance. Thus, **prediction accuracy** of g is the first metric we evaluate. We next discuss multiple functionally-grounded metrics [17] that evaluate the learnt concept dictionary Φ from an interpretability perspective and its use in visualization, including two novel metrics in the context of evaluating CoINs (“faithfulness” and “consistency”).

Fidelity of reconstruction Since reconstructed output plays a crucial role in our visualization pipeline, we evaluate how well does G reconstruct the input. We do so by computing averaged per-sample mean squared error (MSE), perceptual distance (LPIPS) [82] and distance of overall distributions (FID) [28] of reconstructed images \tilde{x} and original input images x .

Faithfulness of concept dictionary Φ The aspect of *faithfulness* for a generic interpretation method asks the question “are the features identified in the interpretation *truly* relevant for the prediction process?” [7, 52]. This is generally computed via simulating “feature removal” from the input and observing the change in predictor’s output [27]. Simulating feature removal from input is relatively straightforward for saliency methods compared to concept-based methods, for example by setting the pixel value to 0. For CoIN systems, this is significantly more tricky, as concept activations $\phi_k(x)$ don’t represent the input x exactly. However, through the decoder, we can evaluate if the concepts identified as relevant for an input encode information that is important for prediction. We adopt an approach similar to a previous proposal of faithfulness evaluation for audio interpretation systems [52]. Concretely, for a given sample x with activation $\Phi(x)$, predicted class \hat{c} and a threshold τ , we first manipulate $\Phi(x)$ such that $\phi_k(x)$ is set to 0 if $r_k(x) > \tau, \forall k \in \{1, \dots, K\}$. That is, we “remove” all concepts with relevance greater than some threshold. This modified version of $\Phi(x)$ is referred to as $\Phi_{rem}(x)$. To compute faithfulness for a given x , denoted by FF_x , we compute the change in probability of the predicted class from original reconstructed sample $\tilde{x} = G(\Omega(\Phi(x), \Phi'(x)))$ to new sample $x_{rem} = G(\Omega(\Phi_{rem}(x), \Phi'(x)))$, that is, $FF_x = g(\tilde{x})_{\hat{c}} - g(x_{rem})_{\hat{c}}$. Ideally, we expect to see a drop in probability ($FF_x > 0$) if the set of relevant concepts “truly” encode information relevant for classification. Following [52] we report the median of FF_x over the test data for different thresholds $0 < \tau < 1$.

Consistency of visualization We expect during visualization of a given concept ϕ_k that a user observes similar semantic modifications across different images. Thus, we hypothesize that if modifying any specific concept activation $\phi_k(x)$ leads to consistent changes for different samples x , then generated output for two versions of $\Phi(x)$, one with $\phi_k(x)$ set to a large value and one with $\phi_k(x) = 0$, should be separable in the embedding space of f (all other concept activations unchanged). In other words, embeddings for images with high $\phi_k(x)$ and low $\phi_k(x)$ should be well separated. To compute this metric, we first create a dataset of generated images with two different sets of activations. For each of training and test set, this is done by first selecting a set of N_{cc} samples for which ϕ_k is highly activating and relevant for. Then we find its maximum activation

ϕ_k^{max} among these samples, and create two generated outputs for each of N_{cc} samples, one x_k^+ such that $\phi_k(x_k^+)$ is set to $\lambda\phi_k^{max}$ with $\lambda \geq 1$, and the other x_k^- such that $\phi_k(x_k^-) = 0$. The two sets of generated images are then gathered into a single dataset $\mathcal{S}_k = \{(x_k^+, 1), (x_k^-, 0)\}$ such that $|\mathcal{S}_k| = 2N_{cc}$, and we learn a binary classifier $\varphi_k : \mathcal{X} \rightarrow \{0, 1\}$, from pooled feature maps of intermediate embedding of f . We train for binary classification for sets created from training data $\mathcal{S}_k^{\text{train}}$ and test on sets created from test data $\mathcal{S}_k^{\text{test}}$. Our *concept consistency* metric CC_k for a given concept k is thus obtained as the accuracy of the binary classifier on $\mathcal{S}_k^{\text{test}}$:

$$CC_k(\mathcal{S}_k^{\text{test}}; \varphi_k) = \frac{1}{2N_{cc}} \sum_{(x_k^+, x_k^-) \in \mathcal{S}_k^{\text{test}}} \varphi_k(x_k^+) + (1 - \varphi_k(x_k^-)) \quad (6)$$

This performance is tabulated for each concept k for a fixed λ , and mean and standard deviation across all concepts is reported.

Baselines The primary comparison methods for us are CoINs that learn unsupervised concepts efficiently, even for large-scale images, FLINT [51] and FLAEM [59]. SENN [7] suffers from computational issues for large-scale images as it requires to compute jacobian of concept dictionary w.r.t input pixels for its loss computation. Thus, for all the metrics we compare with FLINT and FLAEM as our primary baselines. Additionally, for accuracy evaluation, we track the performance of our pretrained classifier f . Note that f (ResNet50) is not an interpretable model and trained entirely for accuracy. Lastly, for faithfulness we compare with a “random” baseline that randomly selects concepts for whom activation is set to 0. Since there is no notion of threshold in selection, in order to make it comparable for a given threshold, we select the same number of concepts randomly as we would for our method. Our proposed system for all evaluations is abbreviated as VisCoIN (Visualizable CoIN).

4.2 Results and discussion

Quantitative results Tab. 1a reports the test accuracy of all the evaluated systems. Our proposed system, VisCoIN performs competitively with the pretrained f considered uninterpretable and purely trained for performance. It also performs better than the other recent CoIN systems for more complex classification tasks (CUB-200 and Stanford Cars) with large number of classes and diverse images. Metrics quantifying the fidelity of reconstruction on test data are in Tab. 2a. The other baselines only optimize for pixel-wise reconstruction and FLINT achieves a lower MSE than VisCoIN. However, crucially, reconstruction from our method approximates the input data considerably better, in terms of perceptual similarity (LPIPS) and overall distribution (FID), which highly contributes to better viewability. Tab. 2b tabulates the median faithfulness FF_x for the evaluated systems on 1000 random test samples for different thresholds. The performance of *Random* baseline being close to 0 even for small thresholds indicates that a random selection of concepts often contains little information relevant for classification of the predicted class. In contrast, concepts identified

Table 1: (a) Accuracy (in %) of interpreter g of CoIN systems, and of the baseline pretrained classifier f . (b) Mean and standard deviation for consistency CC_k over all concept functions ϕ_k (binary accuracy in %).

(a) Accuracy of interpreter g					(b) Consistency of changes			
Dataset	Original- f	FLINT	FLAEM	VisCoIN (Ours)	Dataset	FLINT	FLAEM	VisCoIN (Ours)
CelebA-HQ	<u>87.71</u>	87.25	88.18	<u>87.71</u>	CelebA-HQ	<u>82.6 ± 22.7</u>	57 ± 17.3	85.5 ± 13.9
CUB-200	80.56	77.2	51.76	<u>79.44</u>	CUB-200	<u>72.6 ± 18</u>	55.6 ± 13.6	85 ± 8.4
Stanford Cars	82.28	75.95	50.02	<u>79.89</u>	Stanford Cars	<u>70 ± 16.3</u>	54.9 ± 13.3	82.7 ± 8.3

Table 2: (a) Reconstruction quality (MSE, LPIPS and FID) of CoIN systems. Lower is better. (b) Faithfulness (median FF_x) of CoIN systems and random baseline, for different threshold. Higher is better. Best performance is in **bold**, second best in underline.

(a) Reconstruction quality					(b) Faithfulness					
Dataset	Metric	FLINT	FLAEM	VisCoIN (Ours)	Dataset	Thresh. τ	Random	FLINT	FLAEM	VisCoIN (Ours)
CelebA-HQ	MSE	0.051	0.119	<u>0.094</u>	CelebA-HQ	0.1	0.03	<u>0.254</u>	0.091	0.267
	LPIPS	<u>0.533</u>	0.688	0.405		0.2	0.018	0.201	0.151	<u>0.171</u>
	FID	<u>30.45</u>	39.73	8.55		0.4	0.005	0.07	0.107	<u>0.074</u>
CUB-200	MSE	0.113	0.217	<u>0.161</u>	CUB-200	0.1	<u>0.034</u>	0.004	< 10 ⁻³	0.251
	LPIPS	<u>0.712</u>	0.75	0.545		0.2	<u>0.007</u>	0.002	< 10 ⁻³	0.146
	FID	53.16	<u>51.15</u>	15.85		0.4	<u>0.001</u>	< 10 ⁻³	< 10 ⁻³	0.044
Stanford Cars	MSE	0.121	0.278	<u>0.179</u>	Stanford Cars	0.1	<u>0.035</u>	0.001	< 10 ⁻³	0.161
	LPIPS	<u>0.697</u>	0.734	0.488		0.2	<u>0.016</u>	< 10 ⁻³	< 10 ⁻³	0.118
	FID	<u>64.16</u>	69.44	6.77		0.4	<u>0.002</u>	< 10 ⁻³	< 10 ⁻³	0.034

relevant as part of g in VisCoIN tend to encode information about input that noticeably affects classification. In regard to other CoINs, while the faithfulness results are competitive on CelebA-HQ, for more complex datasets, concept dictionary in VisCoIN is significantly more faithful than FLINT or FLAEM, which do not demonstrate more faithfulness than the *Random* baseline. Finally, the mean and standard deviation for consistency of all concepts is reported in Tab. 1b with $\lambda = 2$. Concepts learnt with VisCoIN demonstrate a higher mean consistency compared to baselines. The deviation across concepts is also lower for our method. We also evaluate consistency with higher values of λ and observe increased separation with better classification performance (Appendix C).

Qualitative results Fig. 4 shows visualization for different class-concept pairs across the three datasets that are determined to have high global relevance $r_{k,c}$ through predictive structure of $g(x)$, as described in Sec. 3.5. For each class-concept pair, we show two maximum activating training samples for the concept from the corresponding class, the reconstructed input from $\Phi(x)$ ($\lambda = 1$) and the generated output with modified concept activation $\phi_k(x)$ by a factor $\lambda = 4$. In all the illustrations, increasing the activation of the concept, *i.e.* moving from $\lambda = 1$ to 4, strongly emphasizes some specific concept in the generated output that can be clearly grounded to the input. For instance, increasing the activation of concept for “Red-eye” in Fig. 4a increases the size of red eye of the bird, a key

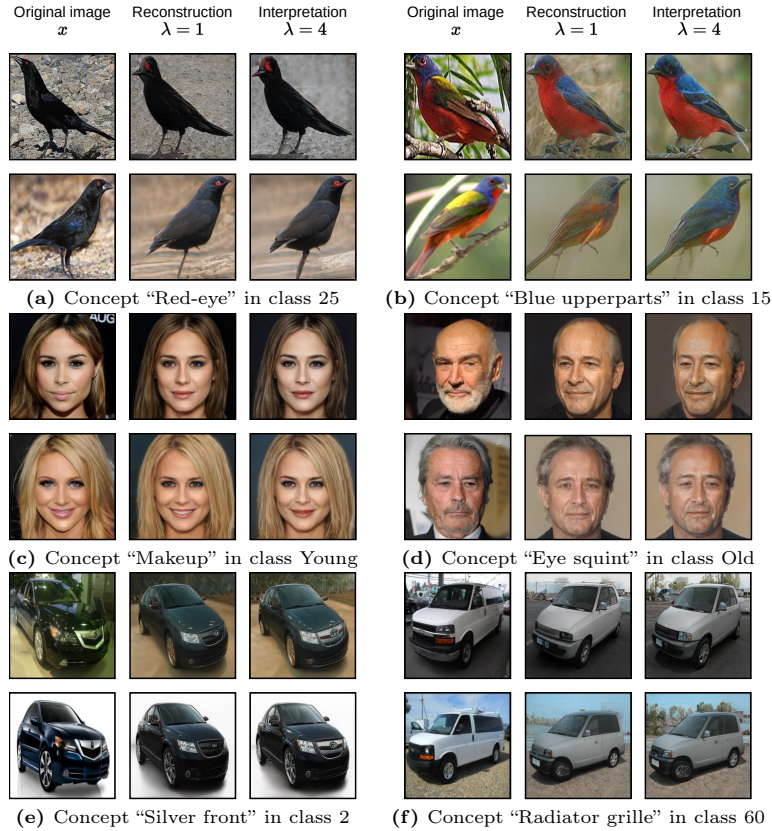


Fig. 4: Qualitative examples obtained for different concepts, classes on (a)-(b) CUB-200, (c)-(d) CelebA-HQ, (e)-(f) Stanford-Cars datasets. On each subfigure, first column corresponds to maximum activated samples x for class-concept pairs with high relevance ($r_{k,c} > 0.5$), second column to reconstructed image obtained with original $\Phi(x)$, and third column to the image obtained by imputing $4 \times \phi_k(x)$ in $\Phi(x)$.

feature of samples from class 25 (“Bronzed-cowbird”). We can also qualitatively verify that the reconstruction has a high enough quality that allows us to “view” the input sample through the generated output and ground the modifications in generated output to the input. However, we also observed that learnt concept functions can be prone to modifying more than one high-level feature in the image. For, *e.g.*, in Fig. 4d, increasing the concept activation increases both “eye-squint” and “beard” in the generated output. A longer discussion about this and other limitations is available in Appendix F.

Ablation study We ablate multiple aspects of our system, with detailed results in Appendix D. Most notably, we observed a tradeoff induced by strength of reconstruction-classification loss (weight γ). A high γ positively impacts the faithfulness but negatively impacts the perceptual similarity of reconstruction.

5 Conclusion

We introduced a novel architecture for *Visualizable CoIN (VisCoIN)*, that addresses major limitations to visualize unsupervised concept dictionaries learnt in CoIN systems for large-scale images. Our architecture integrates the visualization process in the pipeline of the model training, by leveraging a pretrained generative model using a *concept translator* module. This module maps concept representation to the latent space of the fixed generative model. During training, we additionally enforce a viewability property that promotes reconstruction of high-quality images through the generative model. Finally, we defined new evaluation metrics for this novel interpretation pipeline, to better align evaluation of concept dictionaries and interpretations provided to a user. Future works include adapting the design of this system for other type of generative models, or applying it to different visual domains.

References

1. Abdal, R., Qin, Y., Wonka, P.: Image2stylegan: How to embed images into the stylegan latent space? In: Proceedings of the IEEE/CVF International Conference on Computer Vision. pp. 4432–4441 (2019) [7](#), [22](#)
2. Achibat, R., Dreyer, M., Eisenbraun, I., Bosse, S., Wiegand, T., Samek, W., Lapuschkin, S.: From "where" to "what": Towards human-understandable explanations through concept relevance propagation. arXiv preprint arXiv:2206.03208 (2022) [4](#)
3. Adel, T., Ghahramani, Z., Weller, A.: Discovering interpretable representations for both deep generative and discriminative models. In: International Conference on Machine Learning. pp. 50–59. PMLR (2018) [2](#)
4. Agarwal, R., Frosst, N., Zhang, X., Caruana, R., Hinton, G.: Neural additive models: Interpretable machine learning with neural nets. arXiv preprint arXiv:2004.13912 (2020) [4](#)
5. Al-Shedivat, M., Dubey, A., Xing, E.: Contextual explanation networks. arXiv preprint arXiv:1705.10301 (2017) [2](#), [4](#)
6. Alaluf, Y., Patashnik, O., Cohen-Or, D.: Restyle: A residual-based stylegan encoder via iterative refinement. In: Proceedings of the IEEE/CVF International Conference on Computer Vision. pp. 6711–6720 (2021) [7](#)
7. Alvarez-Melis, D., Jaakkola, T.: Towards robust interpretability with self-explaining neural networks. In: Advances in Neural Information Processing Systems (NeurIPS). pp. 7775–7784 (2018) [2](#), [4](#), [5](#), [11](#), [12](#)
8. Alvarez-Melis, D., Jaakkola, T.S.: On the robustness of interpretability methods. arXiv preprint arXiv:1806.08049 (2018) [1](#)
9. Angelov, P., Kangin, D., Zhang, Z.: Towards interpretable-by-design deep learning algorithms. arXiv preprint arXiv:2311.11396 (2023) [4](#)
10. Ardizzone, L., Kruse, J., Rother, C., Köthe, U.: Analyzing inverse problems with invertible neural networks. In: International Conference on Learning Representations (2018) [21](#)
11. Arrieta, A.B., Díaz-Rodríguez, N., Del Ser, J., Bennetot, A., Tabik, S., Barbado, A., García, S., Gil-López, S., Molina, D., Benjamins, R., et al.: Explainable artificial intelligence (xai): Concepts, taxonomies, opportunities and challenges toward responsible ai. Information fusion **58**, 82–115 (2020) [1](#)

12. Baehrens, D., Schroeter, T., Harmeling, S., Kawanabe, M., Hansen, K., Müller, K.R.: How to explain individual classification decisions. *The Journal of Machine Learning Research* **11**, 1803–1831 (2010) [1](#)
13. Beaudouin, V., Bloch, I., Bounie, D., Cléménçon, S., d’Alché Buc, F., Eagan, J., Maxwell, W., Mozharovskiy, P., Parekh, J.: Flexible and context-specific ai explainability: a multidisciplinary approach. *arXiv preprint arXiv:2003.07703* (2020) [1](#)
14. Böhle, M., Fritz, M., Schiele, B.: B-cos networks: Alignment is all we need for interpretability. In: *Proceedings of the IEEE/CVF Conference on Computer Vision and Pattern Recognition*. pp. 10329–10338 (2022) [2](#)
15. Chen, J., Song, L., Wainwright, M., Jordan, M.: Learning to explain: An information-theoretic perspective on model interpretation. In: *International Conference on Machine Learning*. pp. 883–892. PMLR (2018) [3](#)
16. Colin, J., Fel, T., Cadène, R., Serre, T.: What i cannot predict, i do not understand: A human-centered evaluation framework for explainability methods. *Advances in Neural Information Processing Systems* **35**, 2832–2845 (2022) [2](#)
17. Doshi-Velez, F., Kim, B.: Towards a rigorous science of interpretable machine learning. *arXiv preprint arXiv:1702.08608* (2017) [11](#)
18. Esser, P., Rombach, R., Ommer, B.: A disentangling invertible interpretation network for explaining latent representations. In: *Proceedings of the IEEE/CVF Conference on Computer Vision and Pattern Recognition*. pp. 9223–9232 (2020) [21](#)
19. Farid, K., Schrodi, S., Argus, M., Brox, T.: Latent diffusion counterfactual explanations. *arXiv preprint arXiv:2310.06668* (2023) [4](#)
20. Fel, T., Picard, A., Bethune, L., Boissin, T., Vigouroux, D., Colin, J., Cadène, R., Serre, T.: Craft: Concept recursive activation factorization for explainability. In: *Proceedings of the IEEE/CVF Conference on Computer Vision and Pattern Recognition*. pp. 2711–2721 (2023) [4](#)
21. Gautam, S., Boubekki, A., Hansen, S., Salahuddin, S.A., Jenssen, R., Höhne, M., Kampffmeyer, M.: Protovae: A trustworthy self-explainable prototypical variational model. *arXiv preprint arXiv:2210.08151* (2022) [2](#), [4](#)
22. Ghandeharioun, A., Kim, B., Li, C.L., Jou, B., Eoff, B., Picard, R.: Dissect: Disentangled simultaneous explanations via concept traversals. In: *International Conference on Learning Representations* (2021) [4](#)
23. Ghorbani, A., Wexler, J., Zou, J.Y., Kim, B.: Towards automatic concept-based explanations. In: *Advances in Neural Information Processing Systems (NeurIPS)*. pp. 9277–9286 (2019) [4](#)
24. Grigoryev, T., Voynov, A., Babenko, A.: When, why, and which pretrained gans are useful? In: *International Conference on Learning Representations* (2022) [10](#), [24](#)
25. Härkönen, E., Hertzmann, A., Lehtinen, J., Paris, S.: Ganspace: Discovering interpretable gan controls. *Advances in Neural Information Processing Systems* **33**, 9841–9850 (2020) [7](#)
26. He, K., Zhang, X., Ren, S., Sun, J.: Identity mappings in deep residual networks. In: *European conference on computer vision*. pp. 630–645. Springer (2016) [10](#), [22](#)
27. Hedström, A., Weber, L., Krakowczyk, D., Bareeva, D., Motzkus, F., Samek, W., Lapuschkin, S., Höhne, M.M.C.: Quantus: An explainable ai toolkit for responsible evaluation of neural network explanations and beyond. *Journal of Machine Learning Research* **24**(34), 1–11 (2023) [11](#)
28. Heusel, M., Ramsauer, H., Unterthiner, T., Nessler, B., Hochreiter, S.: Gans trained by a two time-scale update rule converge to a local nash equilibrium. *Advances in neural information processing systems* **30** (2017) [11](#)

29. Huh, M., Zhang, R., Zhu, J.Y., Paris, S., Hertzmann, A.: Transforming and projecting images into class-conditional generative networks. In: *Computer Vision–ECCV 2020: 16th European Conference, Glasgow, UK, August 23–28, 2020, Proceedings, Part II* 16. pp. 17–34. Springer (2020) [7](#)
30. Karras, T., Aila, T., Laine, S., Lehtinen, J.: Progressive growing of gans for improved quality, stability, and variation. In: *International Conference on Learning Representations* (2018) [10](#), [23](#)
31. Karras, T., Aittala, M., Hellsten, J., Laine, S., Lehtinen, J., Aila, T.: Training generative adversarial networks with limited data. *Advances in neural information processing systems* **33**, 12104–12114 (2020) [6](#), [7](#), [10](#), [21](#), [22](#), [23](#)
32. Karras, T., Aittala, M., Laine, S., Härkönen, E., Hellsten, J., Lehtinen, J., Aila, T.: Alias-free generative adversarial networks. *Advances in Neural Information Processing Systems* **34**, 852–863 (2021) [7](#)
33. Karras, T., Laine, S., Aila, T.: A style-based generator architecture for generative adversarial networks. In: *Proceedings of the IEEE/CVF conference on computer vision and pattern recognition*. pp. 4401–4410 (2019) [7](#)
34. Karras, T., Laine, S., Aittala, M., Hellsten, J., Lehtinen, J., Aila, T.: Analyzing and improving the image quality of stylegan. In: *Proceedings of the IEEE/CVF conference on computer vision and pattern recognition*. pp. 8110–8119 (2020) [7](#)
35. Katzir, O., Perepelook, V., Lischinski, D., Cohen-Or, D.: Multi-level latent space structuring for generative control. *arXiv preprint arXiv:2202.05910* (2022) [7](#), [8](#), [23](#)
36. Kim, B., Wattenberg, M., Gilmer, J., Cai, C., Wexler, J., Viegas, F., Sayres, R.: Interpretability beyond feature attribution: Quantitative testing with concept activation vectors (tcav). *arXiv preprint arXiv:1711.11279* (2017) [4](#)
37. Kindermans, P.J., Hooker, S., Adebayo, J., Alber, M., Schütt, K.T., Dähne, S., Erhan, D., Kim, B.: The (un) reliability of saliency methods. In: *Explainable AI: Interpreting, Explaining and Visualizing Deep Learning*, pp. 267–280. Springer (2019) [1](#)
38. Kingma, D.P., Ba, J.: Adam: A method for stochastic optimization. *arXiv preprint arXiv:1412.6980* (2014) [23](#)
39. Kingma, D.P., Welling, M.: Auto-encoding variational bayes. *arXiv preprint arXiv:1312.6114* (2013) [21](#)
40. Koh, P.W., Nguyen, T., Tang, Y.S., Mussmann, S., Pierson, E., Kim, B., Liang, P.: Concept bottleneck models. In: *International Conference on Machine Learning*. pp. 5338–5348. PMLR (2020) [2](#), [4](#)
41. Krause, J., Stark, M., Deng, J., Fei-Fei, L.: 3d object representations for fine-grained categorization. In: *Proceedings of the IEEE international conference on computer vision workshops*. pp. 554–561 (2013) [10](#), [23](#)
42. Kwon, M., Jeong, J., Uh, Y.: Diffusion models already have a semantic latent space. In: *The Eleventh International Conference on Learning Representations* (2023) [21](#)
43. Lang, O., Gandelsman, Y., Yarom, M., Wald, Y., Elidan, G., Hassidim, A., Freeman, W.T., Isola, P., Globerson, A., Irani, M., et al.: Explaining in style: Training a gan to explain a classifier in stylespace. In: *Proceedings of the IEEE/CVF International Conference on Computer Vision*. pp. 693–702 (2021) [4](#), [7](#), [8](#), [21](#), [31](#)
44. Lee, G.H., Jin, W., Alvarez-Melis, D., Jaakkola, T.S.: Functional transparency for structured data: a game-theoretic approach. *arXiv preprint arXiv:1902.09737* (2019) [4](#)
45. Li, O., Liu, H., Chen, C., Rudin, C.: Deep learning for case-based reasoning through prototypes: A neural network that explains its predictions. In: *Proceedings of the AAAI Conference on Artificial Intelligence*. vol. 32 (2018) [4](#)

46. Lipton, Z.C.: The mythos of model interpretability. *Commun. ACM* **61**(10), 36–43 (2018) [21](#)
47. Lundberg, S.M., Lee, S.I.: A unified approach to interpreting model predictions. In: *Advances in Neural Information Processing Systems*. pp. 4765–4774 (2017) [1](#), [2](#), [3](#)
48. Mahendran, A., Vedaldi, A.: Visualizing deep convolutional neural networks using natural pre-images. *International Journal of Computer Vision* **120**(3), 233–255 (2016) [2](#)
49. Montavon, G., Binder, A., Lapuschkin, S., Samek, W., Müller, K.: *Explainable ai: interpreting, explaining and visualizing deep learning*. Springer LNCS **11700** (2019) [1](#)
50. Nguyen, A., Dosovitskiy, A., Yosinski, J., Brox, T., Clune, J.: Synthesizing the preferred inputs for neurons in neural networks via deep generator networks. *Advances in neural information processing systems* **29** (2016) [4](#)
51. Parekh, J., Mozharovskiy, P., d’Alché Buc, F.: A framework to learn with interpretation. In: *Advances in Neural Information Processing Systems (NeurIPS)* (2021) [2](#), [3](#), [4](#), [5](#), [9](#), [12](#), [22](#)
52. Parekh, J., Parekh, S., Mozharovskiy, P., d’Alché Buc, F., Richard, G.: Listen to interpret: Post-hoc interpretability for audio networks with nmf. *Advances in Neural Information Processing Systems* **35**, 35270–35283 (2022) [11](#)
53. Park, Y.H., Kwon, M., Jo, J., Uh, Y.: Unsupervised discovery of semantic latent directions in diffusion models. *arXiv preprint arXiv:2302.12469* (2023) [21](#)
54. Rezende, D.J., Mohamed, S., Wierstra, D.: Stochastic backpropagation and approximate inference in deep generative models. In: *International conference on machine learning*. pp. 1278–1286. PMLR (2014) [21](#)
55. Ribeiro, M.T., Singh, S., Guestrin, C.: Why should i trust you?: Explaining the predictions of any classifier. In: *Proceedings of the 22nd ACM SIGKDD international conference on knowledge discovery and data mining*. pp. 1135–1144. ACM (2016) [1](#), [2](#), [3](#)
56. Richardson, E., Alaluf, Y., Patashnik, O., Nitzan, Y., Azar, Y., Shapiro, S., Cohen-Or, D.: Encoding in style: a stylegan encoder for image-to-image translation. In: *Proceedings of the IEEE/CVF conference on computer vision and pattern recognition*. pp. 2287–2296 (2021) [7](#)
57. Rombach, R., Blattmann, A., Lorenz, D., Esser, P., Ommer, B.: High-resolution image synthesis with latent diffusion models. In: *Proceedings of the IEEE/CVF conference on computer vision and pattern recognition*. pp. 10684–10695 (2022) [21](#)
58. Rudin, C., Chen, C., Chen, Z., Huang, H., Semenova, L., Zhong, C.: *Interpretable machine learning: Fundamental principles and 10 grand challenges*. *Statistic Surveys* **16**, 1–85 (2022) [1](#)
59. Sarkar, A., Vijaykeerthy, D., Sarkar, A., Balasubramanian, V.N.: A framework for learning ante-hoc explainable models via concepts. In: *Proceedings of the IEEE/CVF Conference on Computer Vision and Pattern Recognition*. pp. 10286–10295 (2022) [2](#), [4](#), [5](#), [12](#)
60. Sawada, Y., Nakamura, K.: Concept bottleneck model with additional unsupervised concepts. *IEEE Access* **10**, 41758–41765 (2022) [4](#)
61. Selvaraju, R.R., Cogswell, M., Das, A., Vedantam, R., Parikh, D., Batra, D.: Grad-cam: Visual explanations from deep networks via gradient-based localization. In: *Proceedings of the IEEE International Conference on Computer Vision*. pp. 618–626 (2017) [1](#), [2](#)
62. Sheth, I., Ebrahimi Kahou, S.: Auxiliary losses for learning generalizable concept-based models. *Advances in Neural Information Processing Systems* **36** (2024) [4](#)

63. Simonyan, K., Vedaldi, A., Zisserman, A.: Deep inside convolutional networks: Visualising image classification models and saliency maps. arXiv preprint arXiv:1312.6034 (2013) [3](#)
64. Sohl-Dickstein, J., Weiss, E., Maheswaranathan, N., Ganguli, S.: Deep unsupervised learning using nonequilibrium thermodynamics. In: International conference on machine learning. pp. 2256–2265. PMLR (2015) [21](#)
65. Song, Y., Keller, A., Sebe, N., Welling, M.: Latent traversals in generative models as potential flows. arXiv preprint arXiv:2304.12944 (2023) [7](#), [31](#)
66. Springenberg, J.T., Dosovitskiy, A., Brox, T., Riedmiller, M.: Striving for simplicity: The all convolutional net. arXiv preprint arXiv:1412.6806 (2014) [2](#), [3](#)
67. Sundararajan, M., Taly, A., Yan, Q.: Axiomatic attribution for deep networks. In: Proceedings of the 34th International Conference on Machine Learning-Volume 70. pp. 3319–3328. JMLR. org (2017) [3](#)
68. Tov, O., Alaluf, Y., Nitzan, Y., Patashnik, O., Cohen-Or, D.: Designing an encoder for stylegan image manipulation. ACM Transactions on Graphics (TOG) **40**(4), 1–14 (2021) [9](#)
69. Voynov, A., Babenko, A.: Unsupervised discovery of interpretable directions in the gan latent space. In: International conference on machine learning. pp. 9786–9796. PMLR (2020) [7](#)
70. Wah, C., Branson, S., Welinder, P., Perona, P., Belongie, S.: The caltech-ucsd birds-200-2011 dataset (2011) [10](#), [23](#)
71. Wang, J., Chen, Y., Chakraborty, R., Yu, S.X.: Orthogonal convolutional neural networks. In: Proceedings of the IEEE/CVF conference on computer vision and pattern recognition. pp. 11505–11515 (2020) [9](#)
72. Wu, Z., Lischinski, D., Shechtman, E.: Stylespace analysis: Disentangled controls for stylegan image generation. In: Proceedings of the IEEE/CVF Conference on Computer Vision and Pattern Recognition. pp. 12863–12872 (2021) [7](#), [21](#)
73. Xia, W., Zhang, Y., Yang, Y., Xue, J.H., Zhou, B., Yang, M.H.: Gan inversion: A survey. IEEE Transactions on Pattern Analysis and Machine Intelligence (2022) [7](#), [22](#), [24](#)
74. Xie, D., Xiong, J., Pu, S.: All you need is beyond a good init: Exploring better solution for training extremely deep convolutional neural networks with orthonormality and modulation. In: Proceedings of the IEEE Conference on Computer Vision and Pattern Recognition. pp. 6176–6185 (2017) [9](#)
75. Yao, X., Newson, A., Gousseau, Y., Hellier, P.: Feature-style encoder for style-based gan inversion. arXiv preprint arXiv:2202.02183 (2022) [7](#), [24](#)
76. Yeh, C.K., Kim, B., Arik, S.O., Li, C.L., Ravikumar, P., Pfister, T.: On concept-based explanations in deep neural networks. arXiv preprint arXiv:1910.07969 (2019) [2](#), [4](#)
77. Yoon, J., Jordon, J., van der Schaar, M.: Invase: Instance-wise variable selection using neural networks. In: International Conference on Learning Representations (2018) [4](#)
78. Yosinski, J., Clune, J., Nguyen, A., Fuchs, T., Lipson, H.: Understanding neural networks through deep visualization. arXiv preprint arXiv:1506.06579 (2015) [1](#)
79. Yu, F., Zhang, Y., Song, S., Seff, A., Xiao, J.: Lsun: Construction of a large-scale image dataset using deep learning with humans in the loop. arXiv preprint arXiv:1506.03365 (2015) [10](#), [24](#)
80. Zemni, M., Chen, M., Zablocki, É., Ben-Younes, H., Pérez, P., Cord, M.: Octet: Object-aware counterfactual explanations. arXiv preprint arXiv:2211.12380 (2022) [4](#)

81. Zhang, Q., Nian Wu, Y., Zhu, S.C.: Interpretable convolutional neural networks. In: Proceedings of the IEEE Conference on Computer Vision and Pattern Recognition. pp. 8827–8836 (2018) [4](#)
82. Zhang, R., Isola, P., Efros, A.A., Shechtman, E., Wang, O.: The unreasonable effectiveness of deep features as a perceptual metric. In: Proceedings of the IEEE conference on computer vision and pattern recognition. pp. 586–595 (2018) [8](#), [11](#)

A Design choices considered with the generative model

A.1 Desiderata for generative model

We discuss below the reasoning and requirements governing our choice of generative model G , *i.e.*, a *pretrained StyleGAN2-ADA*.

- The generative model should have the ability to model the input with a low dimensional latent space (compared to input dimensions), since a concept representation is typically much lower dimensional than input. Even so, it must possess a structured latent space so that modifying a concept activation can enable latent traversal for visualization. These requirements discourage the use of invertible neural networks [10, 18], or diffusion models [57, 64] whose structure of latent spaces is still being explored [42, 53]. Furthermore, since we constantly rely on input reconstruction during training, the slow sampling process in diffusion models for large-scale images also hinders their suitability for our use case.
- One crucial role of the generative model is to generate high quality natural images. This is essential not only for better reconstruction of large-scale images, but also crucial to ground any visual modifications in the generated images back to the original input. This encouraged our preference for GANs instead of Variational Auto-Encoders (VAEs) [39, 54], specially for large-scale images.
- The generative model also needs to be able to train in limited data regimes if a pretrained generator is not readily available.

Hence, we opted for a competitive, flexible and widely used generative model, StyleGAN2-ADA [31], shown to have demonstrated high-quality generation for various image domains.

A.2 Defining concepts in stylespace of pretrained StyleGAN

Previous works using StyleGAN for interpretation deliberately choose to use the *Stylespace* as concept dictionary [43], which is considered the most disentangled and interpretable latent space of a StyleGAN [72]. However, in regard to a *by-design interpretable* architecture, there is a crucial issue in using the Stylespace of a pretrained StyleGAN as the concept feature space. Indeed, the size of Stylespace, even for small-scale images, runs into many thousands, which is much larger than the size of typical dictionaries in CoINs (by a factor of 10 to a 100). This directly compromises the interpretable structure of the prediction model [46] with much lower number of classes for prediction. Moreover, since the model is pretrained for generation, the space doesn't have sparse activations, further worsening the issue. Note that with the same reasoning, we considered using the extended latent space \mathcal{W}^+ as concept dictionary unsuitable. The final option that remains is using \mathcal{W} space as our concept dictionary. While at first glance it seems an interesting option, since its size is comparable to concept dictionaries in CoINs, and it is also considered as better structured than \mathcal{W}^+ for

latent traversals [73], inverting images to \mathcal{W} space has been found to be lot more challenging [1]. Doing so under even more constraints such as those of concept dictionaries in CoIN, poses an even harder challenge. Hence, we adhered to the CoIN structure to learn a small dictionary compared to the size of \mathcal{W}^+ . Given the constraints imposed on Φ , we designed the decoding part to prioritize better reconstruction.

B Further system details

B.1 Network architectures

We already discuss in the main text the architectures for f and G , both using standard and widely used models, ResNet50 [26] and StyleGAN2-ADA [31] respectively. f and G are pretrained and fixed during training of VisCoIN. As part of our training we train three subnetworks Ψ, Ω, Θ . We already described Θ in the main text, as consisting of a pooling (maxpool), linear and softmax layers in the respective order. We describe the architecture of Ψ network that operates on hidden layers of f and computes the dictionary activations $\Phi(x)$ and the supporting representation $\Phi'(x)$ and the design of concept translator Ω that maps $(\Phi(x), \Phi'(x))$ to extended latent space \mathcal{W}^+ of StyleGAN to reconstruct x .

Architecture of Ψ Our architecture of Ψ mostly follows proposed architecture of Ψ for FLINT [51] which accesses output of two layers for ResNet18 close to the output layer (output of block 3 and penultimate layer of block 4). The ResNet50 also follows a similar structure with 4 blocks. Each block however contains 3, 4, 3 and 3 sub-blocks termed “bottleneck” respectively. In terms of the set of layers accessed by Ψ for VisCoIN, in addition to the corresponding two layers in ResNet50 (output of block 3 of shape $1024 \times 16 \times 16$, output of penultimate bottleneck layer in block 4 of shape $2048 \times 8 \times 8$), we also access a third layer for improved reconstruction (output of block 2 of shape $512 \times 32 \times 32$). Each layer output is passed through a convolutional layer and brought to a common shape of $512 \times 8 \times 8$, the lowest resolution and feature maps. We then concatenate all the feature maps and create two branches, one that outputs $\Phi(x)$ and the other outputs $\Phi'(x)$. The branch computing $\Phi(x)$ is simply two convolutional and a pooling layer yielding an output shape of $K \times 3 \times 3$, where K is the number of concepts, and each $\phi_k(x)$ is a convolutional map of size 3×3 . Thus, the total number of elements in each $\phi_k(x)$ is $b = 9$. The branch computing support representation $\Phi'(x)$ (unconstrained except by reconstruction) applies two fully connected layers to output same number of elements as in $\Phi(x)$. The usefulness of the support representation $\Phi'(x)$ is analysed in Tab. 7.

Architecture of Ω For translating the concept activations $\Phi(x)$ and the supporting representation $\Phi'(x)$ to the extended latent space, we use the concept translator Ω . As described in the main text, it consists of single fully-connected

layers, one for each latent vector (14 different vectors of size 512 for resolution 256×256). We control prediction of a small subset of latent vectors using Φ' , which are expected to contain minimal classification information. To design which latent vectors to control using Φ' , we relied on findings from the work in [35], which roughly divides the different latent vectors in \mathcal{W}^+ as controlling the coarse, mid and fine level features of the generated image with increasing resolution. The first 4 latent vectors control typically the coarse details, such as view-point, pose or scale. The next 4 roughly control the mid-level details, such as shape or background, while the rest control the fine-level details, such as textures and colours. We expect the relevant features for classification to be controlled mostly by mid-level and fine-level latent vectors, except possibly for the highest resolution where very fine-scaled details are controlled. In particular, we predict the first three and last two style vectors using $\Phi'(x)$, which are expected to contain less relevant information for our concept representation. The rest of the style vectors (9 out of 14 for resolution 256) are predicted from $\Phi(x)$. Note that most of the style vectors are still predicted using $\Phi(x)$ to preserve its importance in reconstruction. Also note that employing single FC layers associates each concept activation with a direction in extended latent space.

B.2 Training details

The steps to train our system on a given dataset can be divided into three modular parts: (1) Obtaining a pretrained classifier f with “strong” performance that can provide high-quality source representations to learn from, (2) Obtaining a pretrained generator G that can approximate well the distribution of the given dataset, and (3) Training of g with VisCoIN using the pretrained f and G . When a pretrained f or G is not easily available, we train them on their respective tasks on the given dataset. Among our 3 datasets, CelebA-HQ [30], CUB-200 [70] and Stanford Cars [41], we easily found a pretrained G for CelebA-HQ. All other combinations of f and G were pretrained. We describe the training details of f , G and VisCoIN below:

Pretraining f We pretrain f for classification on each of our datasets before using it for training VisCoIN. We use Adam optimizer [38] with fixed learning rate 0.0001 on CUB-200 and 0.001 on CelebA-HQ to train f . On Stanford-Cars, we use SGD optimizer with a starting learning rate of 0.1, decayed by a factor 0.1 after 30 and 60 epochs. The training is initialized with pretrained weights from ImageNet in each case, and fine-tuned for 10, 30 and 90 epochs on CelebA-HQ, CUB-200 and Stanford-Cars respectively. In all cases, during pretraining, the images are resized to size 256×256 . The accuracy of f is already reported in the main paper. All of these experiments have been conducted on a single A100 GPU, with a batch size of 64 for CelebA-HQ and 128 for Stanford-Cars dataset and on V100 GPU with a batch size of 32 for CUB-200.

Pretraining G We use a pretrained StyleGAN2-ADA [31] for all our experiments. On CelebA-HQ, we used a pretrained checkpoint available from NVIDIA.

For CUB-200 and Stanford-Cars, we pretrain G ourselves. Note that since we want G to generate images entirely from information provided by $\Phi(x)$, we do not use any class labels when training G . One can face two separate challenges in these limited data regimes. The first is to train G in a stable fashion. Our solution to this, as discussed previously, comes from using the ADA training strategy for StyleGAN2. We also use the official StyleGAN2-ADA Pytorch repository to train our models. A second challenge can come from limitations to training resources since these models might require to be trained with tens of millions of real/dataset images (“shown” to the discriminator) in order to reach high quality generation. This could potentially require training with multiple GPUs for multiple days. We address this issue to a reasonable extent by fine-tuning pretrained checkpoints. We utilize the insights from [24] and fine-tune a checkpoint from ImageNet for CUB-200, and LSUN Cars [79] for Stanford Cars. The choices of these specific models was specifically based on the idea that these datasets were the closest domains we had access of pretrained checkpoints to.

We train the G on a single Tesla V100-32GB GPU with mostly default parameters from the official repository. We only differ in (1) Learning a mapping function (that learns to predict latent vectors from gaussian noise vector) with 2 FC layers and (2) For Stanford cars, we observed a collapse in generation of viewpoints with default training after 600k images shown, thus we reduced the strength of horizontal flip augmentation to 0.1 instead of default 1.

We use a batch size of 16 for training. The GANs are trained only on the training data. The final pretrained model for CUB-200 is obtained after training the discriminator with 2 million real images (21 hours). The final model for Stanford-Cars was obtained after training with 1.8 million dataset images (18.5 hours). The pretrained models achieve an FID of around 9.4 and 8.3 on CUB-200 and Stanford Cars, respectively.

Details for VisCoIN We train for 50K iterations on CelebA-HQ and 100K iterations on CUB-200 and Stanford-Cars. We use Adam optimizer with learning rate 0.0001 for all subnetworks and on all datasets. During training, each batch consists of 8 samples from the training data and 8 synthetic samples randomly generated using G . This practice of utilizing the synthetic samples from G is fairly common for encoder-based GAN inversion systems [73, 75], and an additional advantage for our system to use a pretrained G . Note that the use of fidelity loss with a pretrained f instead of a classification loss on $g(x)$ fits neatly with this, as one cannot obtain any ground-truth annotations for the synthetic samples. The training data samples use a random cropping and random horizontal flip augmentation in all cases. All images are normalized to the range $[-1, 1]$ and have resolution 256×256 for processing. This is the default range and resolution we use for pretraining for f and G too. We have already described the architectures of all our components, pretrained or trained as part of training VisCoIN. We tabulate below in Tab. 3 the hyperparameter values for all our datasets. To limit the amount of hyperparameters to tune, we used a

<https://github.com/NVlabs/stylegan2-ada-pytorch>

fixed $\alpha = 0.5$ (weight for output fidelity loss) and $\beta = 3$ (weight for LPIPS loss) for all datasets. The rationale behind choice of all hyperparameters is discussed in Appendix D, wherein we also present the ablation studies w.r.t to multiple components.

Table 3: Hyperparameters values for VisCoIN

Parameter	CelebA-HQ	CUB-200	Stanford Cars
K – Size of concept dictionary Φ	64	256	256
α – Weight for output fidelity	0.5	0.5	0.5
β – Weight for LPIPS	3.0	3.0	3.0
γ – Weight for reconstruction-classification	0.2	0.1	0.05
δ – Weight for sparsity	2	0.2	0.2

B.3 Evaluation details

Metric computation The median faithfulness is computed over 1000 random samples from the test data. For consistency, we use $N_{cc} = 100, \lambda = 2$, *i.e.*, given any concept ϕ_k , we extract its 100 most activating samples over samples of classes its most relevant for. The constant high activation is twice ($\lambda = 2$) the maximum activation of $\phi_k(x)$ over the pool of 100 samples. Thus the binary training dataset created via samples from training data consists of 200 samples, 100 “positive” samples with high activation of $\phi_k(x)$ and 100 “negative” samples with zero activation $\phi_k(x)$. The binary testing dataset also contains the same number of samples of each type but is created via samples from test data. The feature maps we extract are the output of the second block of the pretrained f (ResNet50), the 22nd convolutional layer. The shape for each feature map is $512 \times 32 \times 32$. We pool them across the spatial axis to obtain an embedding of size 512 for any input sample. The linear classifier we train is a linear SVM. We select its inverse regularization strength C from the set $\{0.01, 0.1, 1.0, 5.0\}$ (lower value is stronger regularization). The parameter is selected using 5-fold cross validation on the created training data.

Baseline implementations We utilize the official codebase available for FLINT and FLAEM for our baseline implementation. For fairness, we use the same number of concepts for both of them. Since our architecture is closer to FLINT, we update and adapt it to implement in similar settings as ours. We use the same f architecture (ResNet50 instead of ResNet18) for both the systems and keep it pretrained and fixed. The Ψ architecture is also similar in that it accesses the same set of hidden layers and has the same structure and depth. For other

<https://github.com/jayneelparekh/FLINT>

https://github.com/anirbansarkar-cs/Ante-hoc_Explainability_Concepts

Table 4: Mean and standard deviation for consistency CC_k over all concept functions ϕ_k (binary accuracy in %), using $\lambda = 3$. Higher is better.

Dataset	FLINT	FLAEM	VisCoIN (Ours)
CelebA-HQ	83.4 \pm 22.9	59.5 \pm 19.2	90.9 \pm 13.8
CUB-200	76.4 \pm 20.8	56.7 \pm 14.1	93.4 \pm 6.2
Stanford Cars	77.3 \pm 19.6	55.2 \pm 13.5	91.6 \pm 6.3

Table 5: Quantitative evaluation (FID) of the visualization obtained for interpretation. Lower is better.

Dataset	FLINT	VisCoIN (Ours)
CelebA-HQ	21.12	9.83
CUB-200	26.55	11.71
Stanford Cars	45.72	8

hyperparameters we use their default settings applied earlier for CUB-200. Implementing FLAEM with same network architecture is more complicated as it deviates considerably from the proposed architecture, thus we mostly use their default settings. In their code, they use a base classifier architecture similar to ResNet101 and use the output of final conv layer as the concept representation. In both cases, we do not modify the decoders. FLAEM uses a simpler decoder that learns 3 deconvolution layers, while FLINT learns a deeper decoder consisting of transposed convolution layers.

C Additional experiments

C.1 Consistency with higher λ

We present the results here for evaluating consistency with a higher value of $\lambda = 3$, compared to the main text where $\lambda = 2$. Thus, the constant high activation of $\phi_k(x)$ used to generate “positive” samples of the dataset is increased further. We thus expect the “separation” in the embedding space to increase and consequently a higher performance CC_k of the binary classifier φ_k for any k . The results for both are presented in Tab. 4. The results confirm that emphasizing the concept indeed makes the visual modifications more stronger and consistent. Moreover, we also observe that increase in consistency of VisCoIN tends to be larger than increase for other CoIN systems.

C.2 Qualitative visualization FID

While qualitatively one can clearly observe the difficulty to understand activation maximization based visualization in FLINT. We further support our claim about the unnaturalness of these visualizations compared to visualization in VisCoIN

Table 6: Effect of the weight γ of the Reconstruction-Classification loss in the total training loss, measured by Faithfulness, LPIPS and FID, on CUB-200. Faithfulness computed with a threshold of 0.2. **Bold** indicates setting selected for our experiments.

γ	Faithfulness	MSE	LPIPS	FID
0	0.001	0.142	0.52	13.11
0.1	0.146	0.161	0.545	15.85
0.2	0.236	0.192	0.607	8.84
0.5	0.24	0.209	0.634	11.54

by computing the distance of distributions of visualizations in FLINT, visualizations in VisCoIN and original data distribution. Note that we can't use any reconstruction metrics as FLINT visualizations don't reconstruct a given input. Instead they initialize using a given maximum activating sample and execute the optimization procedure of activation maximization to maximally activate a $\phi_k(x)$. We thus compute the FID distance between the visualizations and the data distribution. For VisCoIN visualization we select our most extreme value of λ . For FLINT visualization we follow their implementation and run the input optimization procedure for 1000 iterations. Since the FLINT visualizations are relatively lot more expensive to compute (1000 backward passes vs 1 forward pass for VisCoIN), we compute the visualizations for 3 maximum activating samples for random 400 relevant class-concept pairs (with $r_{k,c} > 0.5$). Thus the FIDs are computed between 1200 data samples and corresponding visualizations.

D Ablation studies

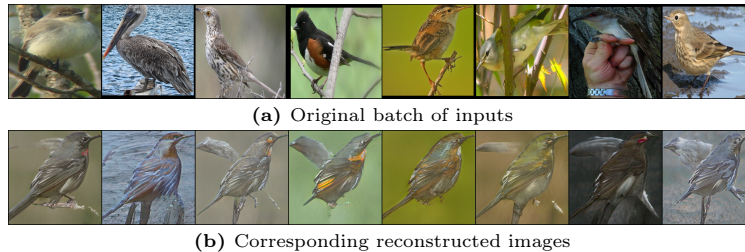
We present ablation studies for components and simultaneously discuss our rationale behind the design selection of these components, (a) effect of reconstruction-classification loss with weight γ , (b) role of using a supporting representation $\Phi'(x)$ to assist in reconstruction, (c) selection of number of concepts K , (d) effect of orthogonality loss, and (e) effect of fidelity and sparsity loss weights.

We highlight at this point to the reader that there is an overarching theme in our various design choices. Most of them are based on shaping the systems suitability for better optimization of perceptual similarity for reconstruction. We constantly aim to achieve better reconstruction without major negative impacts for any other properties. This is because for complex datasets (CUB-200, Stanford Cars), the key bottleneck in the design is to achieve the high-quality reconstruction for viewability.

Reconstruction-classification loss Tab. 6 reports the perceptual similarity and faithfulness with threshold $\tau = 0.2$ on test data of CUB-200 for different strength γ . Interestingly, it indicates a tradeoff between faithfulness and perceptual similarity. Completely removing this loss heavily impacts the faithfulness. However, among the positive γ , our choice was driven strongly by achieving a

Table 7: Effect of using the support representation Φ' , measured by MSE, LPIPS and FID, on CUB-200. **Bold** indicates setting selected for our experiments.

Φ'	K	MSE	LPIPS	FID
Yes	256	0.161	0.545	15.85
No	512	0.178	0.568	13.52
No	256	0.187	0.584	9.55

**Fig. 5:** (a) Final training batch of images shown to the model. (b) Reconstruction obtained using the model trained with $\gamma = 0.2$. Even though FID is better, reconstruction quality is noticeably worse.

reconstruction with high-enough quality and perceptual similarity to enable effective visualization. Thus, we chose $\gamma = 0.1$. The key reason for this is that perceptual similarity is a much better indicator for viewability. For instance, for the $\gamma = 0.2$, even though the FID is better, the reconstruction (LPIPS) is noticeably worse. Reconstruction of the final training batch is indicated in 5, to highlight this issue with high γ . We thus kept a smaller γ for CUB-200 and Stanford Cars where the reconstruction is more challenging and slightly higher value for CelebA-HQ.

Use of support representation Φ' Tab. 7 presents the reconstruction metrics for different concept dictionary sizes and use of Φ' in reconstruction. As before, we prioritized optimization of LPIPS and using Φ' assists in achieving better reconstruction whilst allowing us to employ a smaller dictionary.

Selecting number of concepts K The ablation with different number of concepts is given in Tab. 8 and is an important hyperparameter of the system. While choosing K , it is easy to filter out smaller K values as they clearly lead to a worse reconstruction. However, hypothetically a higher K should improve for all the metrics and thus finding an upper bound for K is more subjective. Our choice was mainly influenced by (1) the observation that increasing from 256 to 512 offered relatively minimal advantage in reconstruction, and (2) previous methods that used supervised concepts train with 312 concepts. Hence we intended to use a similar dictionary size. Since the Stanford Cars dataset had a comparable number of samples and classes, we used the same number of con-

Table 8: Impact of the number of concepts K used in Φ , on accuracy of g (in %), LPIPS and FID, for CUB-200. **Bold** indicates setting selected for our experiments.

K	Accuracy	MSE	LPIPS	FID
512	79.78	0.156	0.537	17.27
256	79.44	0.161	0.545	15.85
128	79.03	0.183	0.578	8.64
64	78.91	0.203	0.624	6.3

Table 9: Impact of orthogonality loss \mathcal{L}_{orth} , on accuracy of g (in %), MSE, LPIPS and FID, for CUB-200. **Bold** indicates setting selected for our experiments.

\mathcal{L}_{orth}	Accuracy	MSE	LPIPS	FID
Yes	79.44	0.161	0.545	15.85
No	79.25	0.171	0.556	9.43

cepts. For CelebA-HQ, we experimented with reduced K as there are only two classes and the images are less diverse compared to the other two datasets.

Orthogonality loss For the final layer of Ψ , we choose a 1×1 convolutional layer. Thus, the weights/kernels for this layer can be represented as single matrix of size number of input feature maps times number of concepts K . We encourage the ℓ_2 normalized columns to be orthogonal which in turn encourages each $\phi_k(x)$ to be predicted using different feature maps. We report the quantitative effect of this loss in Tab. 9. Incorporating this loss offers slight advantage in improved perceptual similarity. However, another key reason we incorporated this loss in our experiments is that we qualitatively observed a greater propensity of multiple concepts highly relevant for a class to capture a common concept about that class. This loss thus offered a way to encourage different concepts to rely on different feature maps. Note that it only affects parameters of final layer of Ψ that outputs $\Phi(x)$, and we do not use any additional hyperparameter for it.

Other loss weights We report the accuracy and reconstruction metrics for different α (weight for output fidelity loss) and δ (weight for sparsity of activations). A small weight on output fidelity impacts the performance of the system and a high weight affects the reconstruction without benefiting the performance much. We found a balance with $\alpha = 0.5$ which we employed for all datasets. A high δ impacts both the performance and reconstruction. For CUB-200 and Stanford Cars, due to prioritizing reconstruction we opted for a smaller $\delta = 0.2$, while for CelebA-HQ, since obtaining a good reconstruction was relatively easier, we opted for a higher $\delta = 2$.

We keep a fixed $\beta = 3$ weight for LPIPS reconstruction loss throughout, for all our datasets and ablations. Even though the system still provides meaningful

Table 10: Effect of weight α on output fidelity loss \mathcal{L}_{of} , measured on accuracy of g (in %), LPIPS and FID, for CUB-200. **Bold** indicates setting selected for our experiments.

α	Accuracy	MSE	LPIPS	FID
0.1	76.9	0.162	0.545	9.37
0.5	79.44	0.161	0.545	15.85
2	79.63	0.187	0.586	7.58

Table 11: Effect of weight δ on sparsity, measured on accuracy of g (in %), MSE, LPIPS and FID, for CUB-200. **Bold** indicates setting selected for our experiments.

δ	Accuracy	MSE	LPIPS	FID
0.2	79.44	0.161	0.545	15.85
2	79.54	0.174	0.562	11.44
20	76	0.201	0.629	9.83

results for $\beta < 3$, the lower values were ruled out mainly because of the importance of a lower perceptual similarity loss, mentioned earlier. The higher values were ruled out because in our initial experiments we observed some instability with high $\beta > 4$. Thus we fixed $\beta = 3$ for all datasets which provided a good balance.

E Additional visualization

We show additional visualizations for different highly relevant class-concept pairs ($r_{k,c} > 0.5$) in Fig. 6. For each class-concept pair, we show the effect of modifying the concept activation on the generated output for three maximum activating training samples. For each sample (on the far-left), we show the corresponding generated outputs for $\lambda = 0$ (center-left), $\lambda = 1$ (center-right) and $\lambda = 4$ (far-right).

Use of difference images can be useful To better highlight regions in the image impacted by modifying concept activations, one can additionally visualize the *differences* between two generated outputs. We show visualizations with the difference in the generated outputs in Fig. 7. Again, we selected highly relevant class-concept pairs ($r_{k,c} > 0.5$), and show the effect of modifying the concept activation on the generated output for three maximum activating training samples. For each sample (on the far-left), we show the corresponding generated outputs for $\lambda = 1$, \tilde{x} (center-left), and $\lambda = 4$, \tilde{x}' (center-right). We then compute and show the difference between the two generated outputs $\tilde{x}' - \tilde{x}$ (far-right). It is worth noting that this exact strategy might not work as effectively for all types of concepts and can require modifications. For example, if “black feathers” are emphasized by a concept, the increasing “black” color won’t be visible in the

difference between \tilde{x}', \tilde{x} . Instead, one could either visualize the reverse difference between \tilde{x}, \tilde{x}' to identify a color being “removed” or visualize the energy of difference for each pixel to identify which regions are modified the most.

F Limitations of approach

- While the idea in principle should be adaptable to other choices of pre-trained G , assuming other choices are inline with desiderata discussed in Appendix A.1, it requires redesigning Ω accordingly. The current VisCoIN design in our experiments is only compatible with StyleGAN.
- As is the case for other CoINs learning unsupervised concepts, the proposed system cannot *guarantee* that concepts precisely correspond to human concepts and not encode other additional information. However, one interesting aspect is that visualization process in VisCoIN gives a better handle at identifying any deviations as visualizations in other unsupervised CoINs can be much harder to understand with granularity for large-scale images.
- While VisCoIN significantly upgrades the visualization pipeline over previous CoIN architectures, some of our choices, arising from restrictions to preserve a by-design interpretable predictive structure or limited computational resources, lead to certain limitations. (1) The choice of using a small dictionary as bottleneck under multiple other constraints leads to worse reconstruction compared to StyleGAN inversion architectures. (2) The choice of using a concept dictionary not defined in the Stylespace, results in learnt concepts that are not as well disentangled as Stylespace. Dictionaries for post-hoc interpretation defined in Stylespace provide more disentangled concepts for interpretation (as in StyleEx [43]), but are significantly larger and thus less suitable for by-design architecture. Finally, (3) the choice of using a pretrained G improves training time, complexity and reusability, but also implies that the system’s quality is limited by the quality of the pretrained G . For instance, for visualization, if G can’t generate some specific feature, it can be difficult to visualize a concept ϕ_k that encodes that feature.
- For the case of single FC layers in Ω our visualization process follows linear trajectories in \mathcal{W}^+ latent space of StyleGAN when modifying an activation. Recent work has shown that linear trajectories are not necessarily optimal for latent traversals [65].

G Potential negative impacts

Given that the understanding of neural network decisions is considered as a vital feature for many applications employing these models, specially in critical decision making domains, we expect our method to have an overall positive societal impact. However, in the wrong hands almost any technology can be misused. In the context of VisCoIN, it can be used to provide deceiving interpretations by corrupting its training mechanisms (for example by training on misleading annotated samples, using deliberately altered pretrained models etc.). Thus, we

expect a responsible use of the proposed methodology to realize its positive impact.

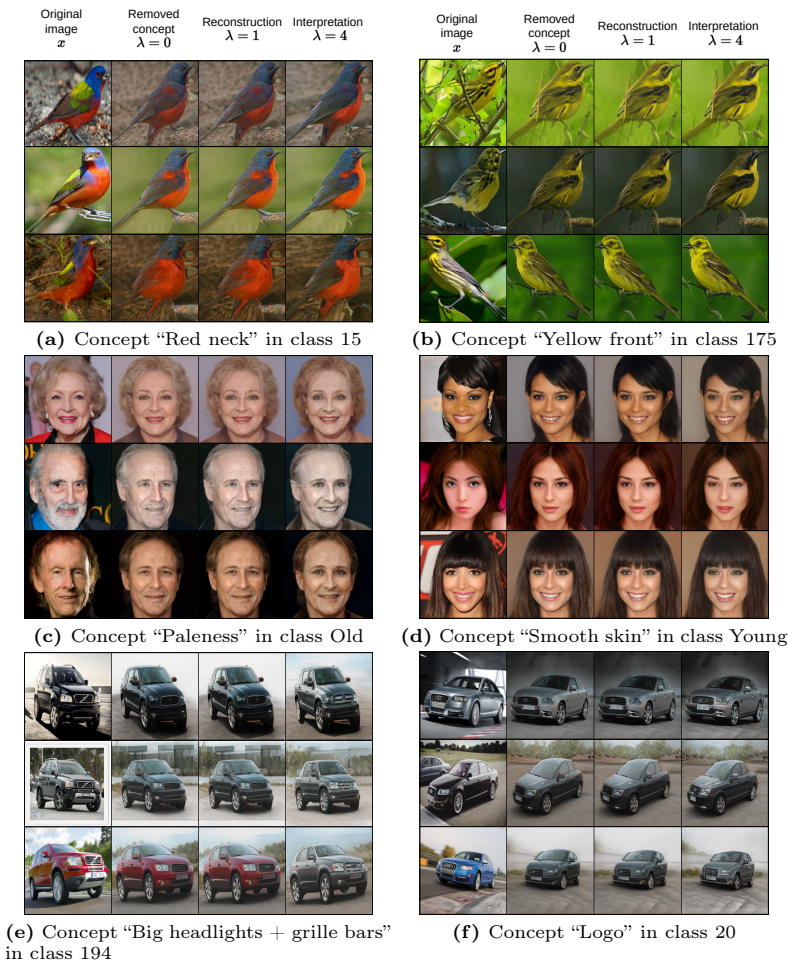


Fig. 6: Additional qualitative examples obtained for different concepts, classes on (a)-(b) CUB-200, (c)-(d) CelebA-HQ, (e)-(f) Stanford-Cars datasets. On each subfigure, first column corresponds to maximum activated samples x for class-concept pairs with high relevance ($r_{k,c} > 0.5$), third column to reconstructed image obtained with original $\Phi(x)$, while second and fourth columns to the images obtained by imputing respectively $\phi_k(x) = 0$ and $4 \times \phi_k(x)$ in $\Phi(x)$.

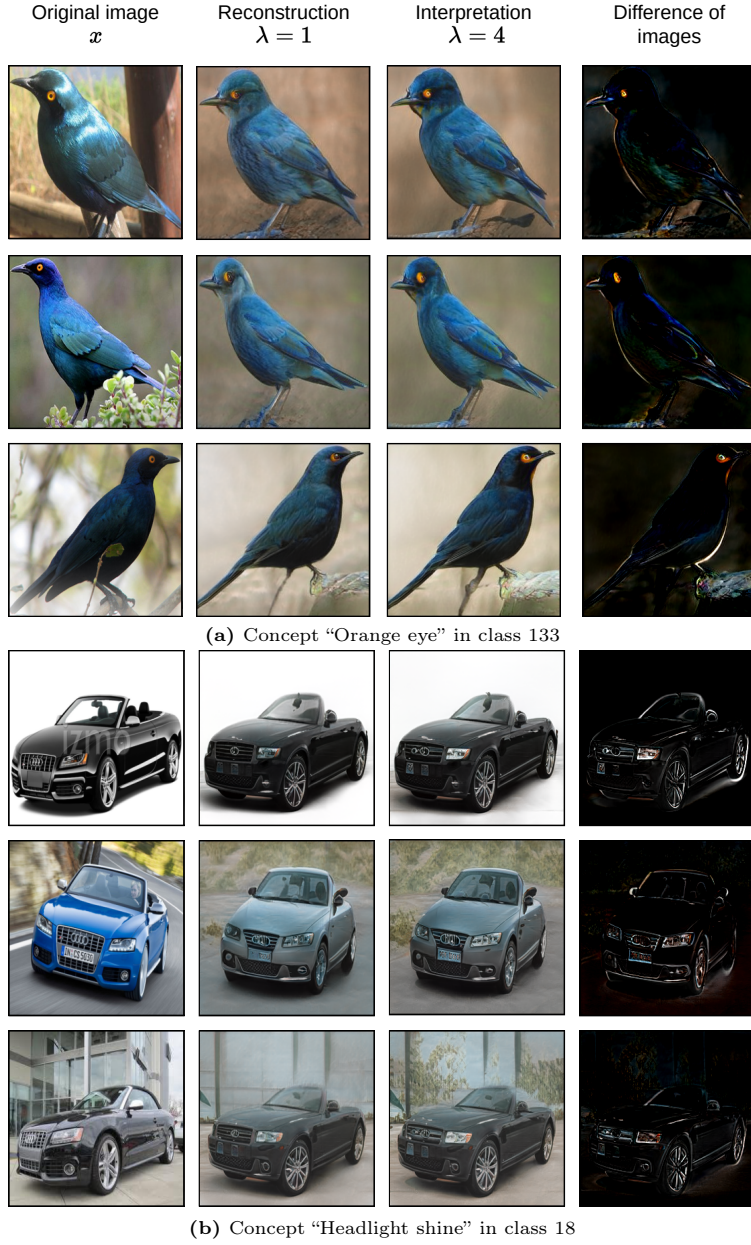


Fig. 7: More qualitative examples obtained for different concepts, classes on (a) CUB-200, (b) Stanford-Cars datasets. On each subfigure, first column corresponds to maximum activated samples x for class-concept pairs with high relevance ($r_{k,c} > 0.5$), second column to reconstructed image obtained with original $\Phi(x)$, third column to the image obtained by imputing $4 \times \phi_k(x)$ in $\Phi(x)$, and fourth column shows the difference between third and second images.